A Eulerian method to analyze wall shear stress fixed points and manifolds in cardiovascular flows

(Article begins on next page)

21 December 2022

A Eulerian method to analyze wall shear stress fixed points and manifolds in cardiovascular flows

8 authors, including:

Valentina Mazzi
Politecnico di Torino
4 PUBLICATIONS   **0** CITATIONS

SEE PROFILE

Diego Gallo
Politecnico di Torino
98 PUBLICATIONS   **929** CITATIONS

SEE PROFILE

Karol Calò
Politecnico di Torino
5 PUBLICATIONS   **2** CITATIONS

SEE PROFILE

Muhammad Owais Khan
University of Toronto
15 PUBLICATIONS   **139** CITATIONS

SEE PROFILE

Some of the authors of this publication are also working on these related projects:

Project Effects of millimetr waves on lipid bilayers View project

Project AXH domain characterization by molecular simulations View project

A Eulerian Method to Analyze Wall Shear Stress Fixed Points and Manifolds in Cardiovascular Flows

The final publication is available at link.springer.com

Valentina Mazzi · **Diego Gallo** · **Karol Cal*ò*** ·
Mehdi Najafi · **Muhammad Owais Khan** ·
Giuseppe De Nisco · **David A. Steinman** · **Umberto
Morbiducci*.**

Abstract Based upon dynamical systems theory, a fixed point of a vector field such as the Wall Shear Stress (WSS) at the luminal surface of a vessel is a point where the vector field vanishes. Unstable/stable manifolds identify contraction/expansion regions linking fixed points. The significance of such WSS topological features lies in their strong link with "disturbed" flow features like flow stagnation, separation and reversal, deemed responsible for vascular dysfunction initiation and progression.
Here we present a Eulerian-based method to analyze WSS topological skeleton through the identification and classification of WSS fixed points and manifolds in complex vascular geometries.
The method rests on the Volume Contraction Theory and analyzes the WSS topological skeleton through the WSS vector field divergence and Poincar*é* index. The method is here applied to computational hemodynamics models of carotid bifurcation and intracranial aneurysm. An in-depth analysis of the time dependence of the WSS topological skeleton along the cardiac cycle is provided, enriching the information obtained from cycle-average WSS. Among the main findings, it emerges that: on the carotid bifurcation, instantaneous WSS fixed points co-localize with cycle-average WSS fixed points for a fraction of the cardiac cycle ranging from 0 to 14.5%; a persistent instantaneous WSS fixed point confined on the aneurysm dome does not co-localize with the cycle-average low WSS region. In conclusion, the here pre-

*Morbiducci U.

Department of Mechanical and Aerospace Engineering, Politecnico di Torino, Corso Duca degli Abruzzi 24, 10129 Turin, Italy
Tel.: +39 011 0906882
Fax: +39 011 5646999
E-mail: umberto.morbiducci@polito.it

Mazzi V. · Gallo D. · Cal*ò* K. · De Nisco G.
Polito^{BIO} Med Lab, Department of Mechanical and Aerospace Engineering, Politecnico di Torino, Turin, Italy

Khan M. O.
Department of Pediatrics, Stanford University, Stanford, CA, USA

Najafi M. · Steinman D. A.
Biomedical Simulation Laboratory, Department of Mechanical & Industrial Engineering, University of Toronto, Toronto, ON Canada

sented approach shows the potential to speed up studies on the physiological significance of WSS topological skeleton in cardiovascular flows, ultimately increasing the chance of finding mechanistic explanations to clinical observations.

Keywords Topological skeleton · Wall Shear Stress divergence · Computational fluid dynamics · Vascular disease · Carotid bifurcation · Intracranial aneurysm

1 Introduction

A large body of literature has demonstrated the importance of Wall Shear Stress (WSS) in the onset and progression of cardiovascular diseases (Malek et al. 1999; Zarins et al. 1983). This frictional force per unit area exerted by the streaming blood on the vascular luminal surface plays a key role in processes involved in vessel wall adaptation and remodeling and leading to vascular dysfunction (Malek et al. 1999; Morbiducci et al. 2016). In all those processes, peculiar WSS phenotypes have been identified as biomarkers of, e.g, endothelial dysfunction, or aneurysm development, growth and rupture (Chung and Cebral 2015). In addition to its role as a biomechanical localizing factor of vascular disease, it has been also suggested that individualized WSS maps might prove useful for clinically monitoring patients, surgical strategies, and post-surgical follow-up care (Fatehi Hassanabad et al. 2019). However, recent evidences have highlighted how the consideration of specific indicators based only upon WSS magnitude and/or direction may oversimplify the complex hemodynamic milieu to which the luminal surface is exposed. In the case of atherosclerosis, it was demonstrated that the exposure to low/oscillatory WSS is a significant but moderately weak predictor of lesions localization (Peiffer et al. 2013b) or endothelial dysfunction at the early stage (Gallo et al. 2018). Similarly, the ability of WSS-based indicators to predict aneurysm wall pathophysiology and remodeling, and to discriminate aneurysms rupture risk, is still debated due to large variations and frequent contradictory results from different studies (Chung and Cebral 2015; Kallmes 2012; Liang et al. 2019). These evidences suggest that an in-depth analysis aimed at identifying more effective WSS-based hemodynamic indicators is needed, to close the gap of knowledge currently limiting the use of WSS as a biomarker for diagnostic and prognostic purposes (Gallo et al. 2016; Morbiducci et al. 2015). In this context, a marked interest recently emerged on WSS fixed points and the stable and unstable manifolds that connect them (Arzani and Shadden 2018; Arzani et al. 2016), forming the topological skeleton of the WSS vector field. Based upon dynamical systems theory, a fixed point of a vector field is a point where the vector field vanishes, and unstable/stable vector field manifolds identify contraction/expansion regions linking the fixed points. The potential link between the WSS topological features and vascular cell biology lies in (1) their ability to quantify the complex and highly dynamic features of the WSS field, and (2) their strong link with flow features like flow stagnation, separation, and recirculation, which are usually classified as "aggravating flow events" and in turn linked to "aggravating biological events". Several studies have looked at the WSS topological skeleton in the context of cardiovascular flows. Fixed points were considered in idealized computational hemodynamic models of coronary bypass grafts to study flow separation (Ethier et al. 2000), in personalized computational models of cerebral aneurysm (Baek et al. 2010; Chien et al. 2008; Gambaruto and João 2012; Goubergrits et al. 2012), and to study the impact of cerebral aneurysm coiling (Goubergrits et al. 2010). WSS fixed points were also identified in computational hemodynamic models of aortic coarctation (Andersson et al. 2017). Interestingly, previous investigations have demonstrated how focal pathological vascular responses might be triggered by

WSS fixed points and by the action of WSS contraction/expansion regions, highlighted by WSS manifolds (Arzani and Shadden 2018). These responses are relevant for atherosclerosis initiation, or aneurysm development and rupture. In particular, WSS manifolds has been linked to near-wall mass transport (Arzani et al. 2016), with implications in atherosclerosis initiation and in general in vascular dysfunction (Ethier 2002). A co-localization between WSS fixed points and wall thinning in cerebral aneurysm domes was reported (Suzuki et al. 2015; Tobe et al. 2014). Moreover, Ge and Sotiropulos (2010) hypothesized a link between WSS fixed points observed on the aortic side of the aortic valve leaflet and the focal distribution of calcification lesions in the valve.

For these reasons, WSS topological skeleton analysis is of great interest and motivates the study herein.

Very recent studies have reinvigorated the interest in WSS topological skeleton analysis (Arzani and Shadden 2016; 2018; Arzani et al. 2016; 2017). On them, Lagrangian-based techniques, based on the so-called Lagrangian Coherent Structures approach, have been proposed to identify WSS manifolds (Arzani et al. 2016). Although Lagrangian-based approaches are typically preferred to reveal and understand inherently transient hemodynamic conditions from a fluid mechanics perspective (Shadden and Arzani 2015), their extensive use might have some practical limitations, namely the computational costs, the poor control over the flow region of interest, and the application of higher-order integration schemes, being based on integrated trajectory information (Reza and Arzani 2019). On the other hand, a Eulerian-based, trajectory-free method, recently proposed to approximate invariant manifolds, has been applied only to 2D analytical vector fields (with possible extension to higher dimensions) (Nave and Ross 2017).

Moving from the recent interest on the role of WSS topological skeleton in vascular dysfunction, and on effective methods for its calculation, in the present methodological study we introduce a Eulerian method for identifying WSS topological skeleton on the luminal surface of 3D vessels. This Eulerian method, needing only of single snapshots of the WSS vector field, is faster and less expensive to compute than those Lagrangian techniques that have become popular tools (Arzani et al. 2016). We propose a novel application of the Volume Contraction Theory in cardiovascular flows, demonstrating that the divergence of the WSS vector field gives information about the associated dynamical system. In particular, here we demonstrate that stable and unstable manifolds can be easily captured through the divergence of the normalized WSS vector field. The proposed methodology, avoiding numerical integration for manifolds identification as required for Lagrangian-based approaches, allows a practical implementation with reduced computational costs. To complete the analysis, a robust, automatic method for WSS fixed points identification and classification on 3D complex geometries is proposed, based on Poincaré index and Jacobian analysis. The present method allows to identify WSS manifolds and WSS fixed points separately, thus offering the benefits of modularity. The Eulerian-based practical method presented here can be easily adopted to focus on WSS topological skeleton analysis along the cardiac cycle. The proposed methods are applied here to personalized computational hemodynamic models of one carotid bifurcation and one intracranial aneurysm to explore their potential usefulness on cardiovascular districts characterized by distinguishable "disturbed" flow features.

2 Theoretical remarks

In this section, a brief theoretical background is reported for a better understanding of the theory supporting the proposed method. We refer the interested reader to (Argyris et al. 2015) for a broader overview of this topic.

### 2.1 Dynamical systems and Volume Contraction Theory

Here the basic concepts of dynamical systems theory, enabling the analysis of complex phenomena is provided. A dynamical system is defined as a set of n differential equations:

$$\dot{\mathbf{x}} = \mathbf{F}(t, \mathbf{x}), \tag{1}$$

where $\mathbf{x}(t) = \Phi^{t_0}(t, \mathbf{x}_0)$ is a function ($\mathbf{x} \in \mathbb{R}^n$) depending on time $t \in \mathbb{R}^+$ and on the initial condition $\mathbf{x_0} = \mathbf{x}(t_0) \in \mathbb{R}^n$ and it is everywhere tangent to the n-dimensional vector field $\mathbf{F}$. In general, eq. (1) describes the time derivative of a trajectory $\mathbf{x}(t)$ on the phase space and the vector field $\mathbf{F}$ provides the velocity of the dynamical system. Dynamical systems are usually not explicitly solvable and the solutions can be markedly complex/chaotic. For these reasons, the focus of the dynamical systems theory is not on finding precise solutions to the equations, but conversely the theory is concerned with topological skeleton identification. Topological skeleton is one of the most important features of a vector field and it is composed by the fixed points and their connection, called stable/unstable manifolds. Roughly speaking, a fixed point of a vector field is a critical point where the vector field vanishes. The nature of a fixed point can be either stable or unstable. A stable point attracts all trajectories that start close to it, while an unstable point repels trajectories starting close to it. Moreover, a fixed point can be classified as a node, a focus or a saddle point. In Figure 1 the fixed points classification is presented. Saddle-type fixed points are of particular interest since typically, the manifold starts from a saddle point and vanish into a stable node or a stable focus. Stable and unstable manifolds associated with a saddle-type fixed point are composed by all trajectories that tend to the fixed point asymptotically. The unstable manifold attracts nearby trajectories, as opposed to the stable manifold, that repels nearby trajectories.

The analysis of dynamical systems can be performed by applying the Volume Contraction theory, based on methods inspired by fluid mechanics and differential geometry and providing an elegant and simple way to analyse the behaviour of dynamical systems. The theory is based on the study of the evolution of infinitesimal volumes in a neighbourhood of attractors. In the mathematical description of a dynamical system, an attractor is a set of phase states towards which the system tends to evolve, independent of the initial conditions. Each attractor has a basin of attraction containing the initial conditions, generating all possible trajectories converging to itself. The simplest attractors are stable fixed points (Figure 1). The main objective of the Volume Contraction theory is to determine the temporal change of an elemental volume dV in the dynamical system phase space. In details, given the dynamical system, represented in eq. (1), and an arbitrary closed surface $S(t) = \partial V(t)$ of a volume $V(t)$ in the phase space, $S(t)$ evolves during the time interval dt, thus resulting in a change of volume (i.e., expansion or contraction, Figure 2) in the phase space, which can be expressed as follows:

$$\frac{dV(t)}{dt} = \int\int_S \mathbf{F} \cdot \mathbf{n} dS = \int\int\int_V \nabla \cdot \mathbf{F} dV, \tag{2}$$
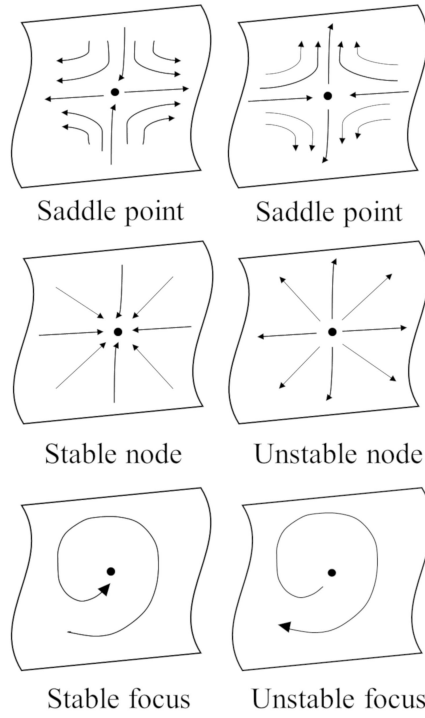
Fig. 1 Classification of fixed points in a vector field. For a saddle point (top row), streamlines of the surrounding vector field appear to intersect themselves. Nodes (middle row) are characterized by converging or diverging streamlines in all directions and based on this are classified in stable or unstable, respectively. Foci (bottom row) are characterized by spiraling streamlines in their surroundings and, like nodes, they are classified as stable or unstable according to their attracting or repelling nature, respectively

where $\mathbf{n}$ is the unit normal to the surface S and the right equality is the consequence of the application of the Gauss Theorem.

It has been demonstrated in general terms (Lévêque 1928), and recently reinforced in relation to cardiovascular flows (Gambaruto et al. 2010), that the velocity vector over a wall can be expressed in terms of WSS vector as follows:

$$\mathbf{u}_\pi = \frac{\tau \partial n}{\mu} + O(\partial n^2) = \kappa \tau + O(\partial n^2), \tag{3}$$

where $\mathbf{u}_\pi \in \mathbb{R}^3$ is the near-wall velocity, $\tau \in \mathbb{R}^3$ the WSS vector field on the luminal surface of the vessel, μ the dynamic viscosity (assuming a Newtonian behavior for the fluid), ∂n the intravascular distance from the wall, and $\kappa = \partial n / \mu \in \mathbb{R}$. As demonstrated elsewhere (Gambaruto et al. 2010), $\mathbf{u}_\pi$ is predominantly tangential to the wall (the additional component of the velocity normal to the wall being second order in ∂n, can be considered to have a lesser degree of importance in the analysis). Using the expression of the velocity vector $\mathbf{u}$ given by eq. (3) in eq. (2), dividing both equation members by the volume V and in the limit as V approaches zero (i.e., shrinking the near-wall volume V to a point on the luminal surface of
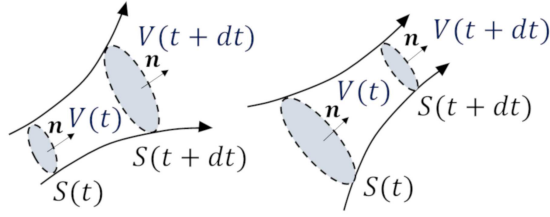
Fig. 2 Volume expansion (left panel) and contraction (right panel) in the phase space of a dynamical system. In case of volume expansion, the arbitrary closed surface $S(t)$ and the corresponding volume $V(t)$ bounded by $S(t)$ increase over time interval dt, while in case of volume contraction decrease over time interval dt

the vessel), it can be written:

$$\lim_{V \to 0} \frac{1}{V} \frac{dV(t)}{dt} = \lim_{V \to 0} \frac{\kappa}{V} \int \int_S \tau \cdot \mathbf{n} dS$$
$$= \lim_{V \to 0} \frac{\kappa}{V} \int \int \int_V \nabla \cdot \tau dV, \qquad (4)$$

where $\mathbf{n}$ is the unit normal to the surface S. From eq. (4) the physical meaning of the divergence operator is derived:

$$\lim_{V \to 0} \frac{1}{V} \int \int_S \tau \cdot \mathbf{n} dS = (\nabla \cdot \tau), \qquad (5)$$

i.e., the local value of the WSS vector divergence is equal to its total flux per unit volume. From eqns. (4) and (5) it follows that the divergence of the vector field characterizes the behavior of the phase space in the infinitesimal neighborhood of a trajectory. In general, the dynamical system is defined non-conservative if $\nabla \cdot \mathbf{F} \neq 0$ in some regions of phase space, meaning that the volume of phase space V is not preserved, and it contracts or expands along time. For a non-conservative system (which is the case object of this study since WSS vector filed is, in general, not conservative even in the case of incompressible flows), trajectories tend to a lower-dimensional subset of the phase space, i.e. to an attractor. In the context of the WSS vector field at the luminal surface of a vessel, this reflects a physical meaning, i.e., a point is called: (1) source if the divergence of the vector field at that point is positive, meaning that locally shear forces play an expansion action on the endothelium; (2) sink if the divergence of the vector field at that point is negative, meaning that locally shear forces play a contraction action on the endothelium.

Starting from eq. (2), the volume contraction rate $\Lambda(t, \mathbf{x})$ of a n-dimensional system (i.e., the volume contraction per unit volume in phase space) can be defined as the rate of separation of infinitesimally close trajectories, as proposed elsewhere (Argyris et al. 2015). For the problem under study, and based on eqns. (4) and (5), $\Lambda(t, \mathbf{x})$ for the WSS vector field can be expressed as follows:

$$\Lambda(t, \mathbf{x}) = \sum_{i=1}^{n} \frac{\partial \tau_i}{\partial x_i} = \nabla \cdot \tau(\mathbf{t}, \mathbf{x}) = tr\, J(\tau) = \sum_{i=1}^{n} \lambda_i, \qquad (6)$$

where J is the Jacobian matrix of τ and λ_i are its eigenvalues. For the aim of this study, the relevant result of this theory is that the volume contraction rate along every trajectory

leading to an attractor is negative. Hence, the WSS vector field divergence can be used to identify the connections between attractors, thus providing the boundaries of the basins of attractions of each attractor. Summarizing, the computation of the divergence of the WSS vector field gives practical information about the associated dynamical system. In particular, the divergence operator is able to (1) encase the connections between attractors and (2) identify the basin of attraction of each attractor, dividing the domain into different regions. In the present work we refer to topological skeleton as the vector field features composed by fixed points and contraction/expansion regions identified through continuous regions of negative/positive value of divergence and approximating unstable/stable manifolds, respectively.

3 Methods

3.1 Computational Hemodynamics

The vascular geometries considered here are part of two broader studies. In detail, one carotid bifurcation model from the Vascular Aging-The Link That Bridges Age to Atherosclerosis (The VALIDATE Study) (Gallo et al. 2018) and one intracranial aneurysm model from the Toronto Western Hospital aneurysm clinic were considered.

Carotid bifurcation geometry and inlet/outlet flow boundary conditions were extracted from contrast-enhanced angiography and phase-contrast MRI, respectively. Details on geometry reconstruction, meshing and CFD simulation where extensively reported elsewhere (Gallo et al. 2015; 2018; Hoi et al. 2010). Briefly, the lumen geometry was reconstructed from its brachiocephalic origin to well above the bifurcation using the open-source Vascular Modelling Toolkit (VMTK, www.vmtk.org). A quadratic tetrahedral mesh of cardinality 1160048 was generated using ANSYS ICEM-CFD software and pulsatile, patient-specific flow waveforms were imposed as boundary conditions at the CCA inlet and ICA outlet sections. Computational fluid dynamics simulation was carried out using a finite element-based in-house solver (Minev and Ross Ethier 1999) and using up to 4800 time steps per cardiac cycle. As regards intracranial aneurysm model, details regarding geometry reconstruction, meshing strategy and CFD settings were presented elsewhere (Chnafa et al. 2018). In particular, VMTK software was used to generate a tetrahedral mesh of cardinality 3315791. Simulation was performed using a minimally-dissipative solver developed within the open-source finite-element-method library FEniCS (Mortensen and Valen-Sendstad 2015) and using up to 10000 time steps per cardiac cycle. A fully developed Womersley velocity profile was applied at the inlet, and outflow division was based on a splitting method presented elsewhere (Chnafa et al. 2018).

The considered intracranial aneurysm model was characterized by the presence of cycle-invariant flow instabilities (Valen-Sendstad and Steinman 2014).

3.2 Practical way for WSS topological skeleton identification

The WSS topological skeleton identification method is sketched in Figure 3. The single steps of the method are detailed in the followings.
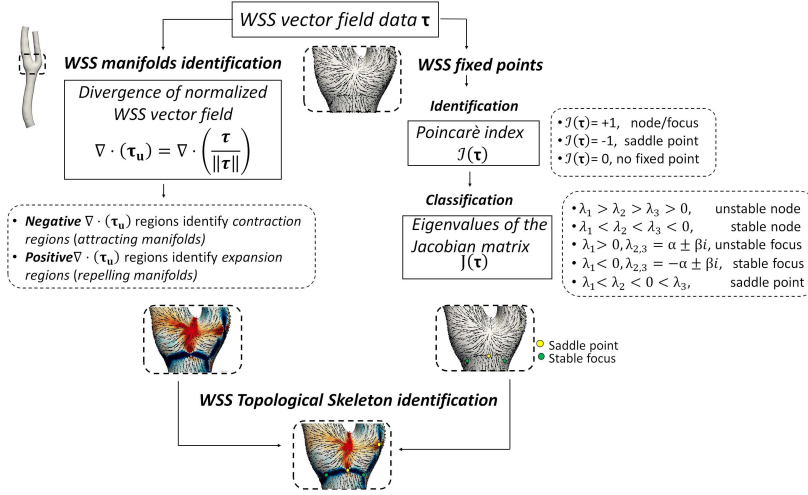
Fig. 3 Workflow of the proposed approach to WSS topological skeleton identification. The skeleton is composed by the WSS manifolds, extracted with the analysis of the divergence of the WSS vector field, and by the WSS fixed points, which are identified by the Poincaré index and then classified by the values of the eigenvalues of the Jacobian matrix. See Figure 11 for the color scale

3.2.1 WSS manifolds identification based on WSS divergence

On WSS data available on the linearized triangle mesh (i.e., the surface of the tetrahedral volume mesh) from the CFD simulations, the divergence operator was applied. In detail, given a generic surface mesh triangle T_η ($\eta = 1,..,N$, where N is the number of mesh triangles), we consider a vertex-based representation of the WSS vector field τ where $\mathbf{x}_\zeta \in \mathbb{R}^3$ is the location of the generic vertex ζ ($\zeta = i,j,k$). The first step of the algorithm is the discretization of the vector field through a piecewise constant vector per mesh triangle face representation.

To do that, the vector field components $(\tau_x)_\zeta, (\tau_y)_\zeta, (\tau_z)_\zeta$ defined on each vertex mesh in a Cartesian reference frame are interpolated in a generic position inside mesh triangle T_η using barycentric coordinates using piecewise linear basis functions B_ζ:

$$\tau_x(\mathbf{p}) = (\tau_x)_i B_i(\mathbf{p}) + (\tau_x)_j B_j(\mathbf{p}) + (\tau_x)_k B_k(\mathbf{p})$$
$$\tau_y(\mathbf{p}) = (\tau_y)_i B_i(\mathbf{p}) + (\tau_y)_j B_j(\mathbf{p}) + (\tau_y)_k B_k(\mathbf{p})$$
$$\tau_z(\mathbf{p}) = (\tau_z)_i B_i(\mathbf{p}) + (\tau_z)_j B_j(\mathbf{p}) + (\tau_z)_k B_k(\mathbf{p}), \tag{7}$$

where $\mathbf{p} = (x,y,z) \subset T_\eta$. The basis functions B_ζ are of the form (Figure 4):

$$B_i(\mathbf{p}) = \frac{A_i}{A_T}, \, B_j(\mathbf{p}) = \frac{A_j}{A_T}, \, B_k(\mathbf{p}) = \frac{A_k}{A_T} \tag{8}$$

where, A_T is the surface area of triangle mesh T_η, and A_i, A_j, A_k are the surface areas of the triangles of coordinates $\{\mathbf{p}, \mathbf{x}_j, \mathbf{x}_k\}$, $\{\mathbf{p}, \mathbf{x}_i, \mathbf{x}_k\}$, $\{\mathbf{p}, \mathbf{x}_i, \mathbf{x}_j\}$, respectively (Figure 4). By construction (Figure 4), $B_i(\mathbf{x}_i) = B_j(\mathbf{x}_j) = B_k(\mathbf{x}_k) = 1$ and $B_i(\mathbf{x}_{j,k}) = B_j(\mathbf{x}_{i,k}) = B_k(\mathbf{x}_{i,j}) = 0$.
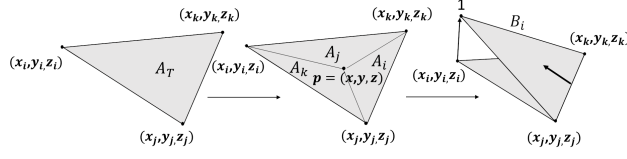
Fig. 4 Piecewise linear basis function B_i

By differentiating the basis functions B_ζ, the gradient of τ_x in $\mathbf{p}$ can be expressed as:

$$\nabla \tau_x(\mathbf{p}) = (\tau_x)_i \nabla B_i(\mathbf{p}) + (\tau_x)_j \nabla B_j(\mathbf{p}) + (\tau_x)_k \nabla B_k(\mathbf{p})$$

$$\nabla \tau_y(\mathbf{p}) = (\tau_y)_i \nabla B_i(\mathbf{p}) + (\tau_y)_j \nabla B_j(\mathbf{p}) + (\tau_y)_k \nabla B_k(\mathbf{p})$$

$$\nabla \tau_z(\mathbf{p}) = (\tau_z)_i \nabla B_i(\mathbf{p}) + (\tau_z)_j \nabla B_j(\mathbf{p}) + (\tau_z)_k \nabla B_k(\mathbf{p}), \tag{9}$$

where $\nabla B_\zeta(\mathbf{p})$ is the steepest ascent direction perpendicular to the opposite edge, expressed as:

$$\nabla B_i(\mathbf{p}) = \frac{\mathbf{n}_{T\eta} \times \mathbf{e}_{jk}}{2 A_T}$$

$$\nabla B_j(\mathbf{p}) = \frac{\mathbf{n}_{T\eta} \times \mathbf{e}_{ki}}{2 A_T}$$

$$\nabla B_k(\mathbf{p}) = \frac{\mathbf{n}_{T\eta} \times \mathbf{e}_{ij}}{2 A_T}, \tag{10}$$

where $\mathbf{n}_{T\eta}$ is the unit vector normal to the triangle surface T_η and $\mathbf{e}_{jk}$, $\mathbf{e}_{ki}$, $\mathbf{e}_{ij}$ denote the edges opposite to vertex i, j, k, respectively (Figure 4).

Combining eq. (9) and eq. (10), the divergence of WSS vector field in $\mathbf{p} \subset T_\eta$ can then be obtained:

$$\nabla \cdot \tau(\mathbf{p}) = \nabla \tau_x(\mathbf{p}) \cdot \hat{\mathbf{x}} + \nabla \tau_y(\mathbf{p}) \cdot \hat{\mathbf{y}} + \nabla \tau_z(\mathbf{p}) \cdot \hat{\mathbf{z}}. \tag{11}$$

The value of $\nabla \cdot \tau$ at each vertex ζ of the mesh triangle T_η is calculated as the average value of the WSS divergence over all triangles of the mesh the considered vertex ζ belongs to:

$$(\nabla \cdot \tau)_\zeta = \frac{\sum_{T_\chi \sim \zeta} (\nabla \cdot \tau)_{T_\chi \sim \zeta}}{\#T_\chi}, \tag{12}$$

where $\#T_\chi$ is the total number of surface mesh triangles the vertex ζ belongs to.

As mentioned before, vector field divergence plays a central role in the Volume Contraction Theory, because this scalar quantity can be used to quantify the rate of separation of close trajectories. However, one limitation could weaken the application of this theory, in particular in those cases where, in spite of a negative value of the vector field divergence, the distance between two neighbouring trajectories increases. This is because in general the divergence of a vector field depends upon the algebraic summation of the magnitude of the single gradients of each vector component along its direction (see eq. (11)), giving rise to situations as the ones depicted in the schematics in Figure 5. Here, in order to avoid ambiguities in using the WSS vector field divergence for manifolds identification (Figure 3),
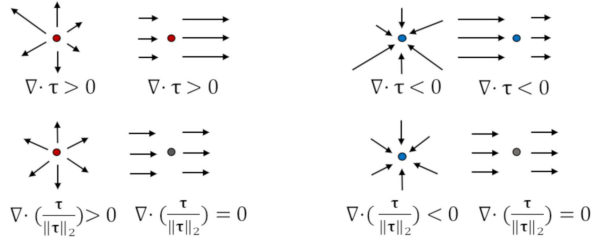
Fig. 5 Comparison between the divergence of different vector field configurations (top) and divergence of different normalized vector field configurations (bottom). The divergence of a normalized vector field allows to exclude the vector field local magnitude variations

the divergence of the normalized WSS vector field, calculated according to eqns from (7) to (12), was considered:

$$\nabla \cdot (\tau_{\mathbf{u}}) = \nabla \cdot \left(\frac{\tau}{\| \tau \|} \right),$$

(13)

where $\tau_{\mathbf{u}}$ is the WSS unit vector. The use of the normalized WSS vector field in eq. (13) allows the identification of the WSS spatial contraction/expansion configuration patterns (i.e., of the WSS manifolds), independent of the vector field local magnitude variations (Figure 5).

3.2.2 WSS fixed points identification and classification

Fixed points and their connections play a central role in the topology of the WSS vector field. Typically, computational data are available as discrete samples at the vertices of a mesh, and the direct application of the theory of dynamical system to sampled data could lead to consistency loss (Bhatia et al. 2014). Here, a robust method to fixed points identification (Figure 3) is proposed. Firstly, identification of fixed points location is performed using the Poincaré index. The relevance of this topological index lies in its mesh-independent and topologically invariant properties. Then, the fixed points identified by the Poincaré index are classified according to their nature (Figure 3). This classification is performed using Jacobian analysis based on the eigenvalues of the linearized vector field, because the Poincaré index allows to identify fixed point locations, but does not provide information about the nature of the fixed point (as summarized in Figure 3).

As an explanatory definition that may help the better understanding of the mathematical concept, here we preliminarily introduce the Poincaré index for a 2D arbitrary vector $\mathbf{v}(\mathbf{x}) = (X(\mathbf{x}), Y(\mathbf{x}))$ with $\mathbf{x} \in \mathbb{R}^2$. Then we consider an isolated fixed point $\mathbf{x_0} \in \mathbb{R}^2$ of vector field $\mathbf{v}$ with a neighborhood N such that there are no fixed points in N other than $\mathbf{x_0}$, so that $\mathbf{x_0}$ and its neighborhood can be ideally inscribed inside a closed curve γ. The Poincaré index $\mathscr{I}(\gamma, \mathbf{v})$ of the curve γ relative to the vector field $\mathbf{v}$ is the number of the positive field rotations while traveling along γ in positive direction:

$$\mathscr{I}(\gamma, \mathbf{v}) = \frac{1}{2\pi} \int_{\Gamma} d\theta = \frac{1}{2\pi} \int_{\Gamma} d\arctan(\frac{Y}{X}),$$

(14)

where θ is the vector field angular variation (Figure 6). The possible Poincaré index values are $+1$, 0 and -1: if $\mathscr{I}(\gamma, \mathbf{v}) = 1$, $\mathbf{x_0}$ is a node or a focus, if $\mathscr{I}(\gamma, \mathbf{v}) = -1$, x_0 is a saddle
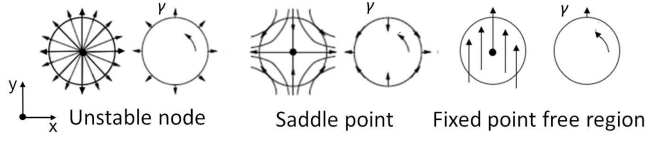
Fig. 6 Unstable node, saddle point and fixed point free region configuration for a arbitrary 2D vector field. While traveling along the closed curve γ in positive direction (as indicated by the arrows inside the curve), the Poincarè index is the number of the positive fields rotations and has value equal to $+1$ for the unstable node in the left panel, -1 for the saddle point exemplified in the middle panel and 0 for a fixed point free region.

point and finally the Poincar$é$ index of a fixed point free region is 0 (Figure 6).

Detection methods of isolated fixed points in analytical or 2D vector fields have been already proposed by several authors (Tricoche et al. 2002). Less work has been done on fixed points detection on vertex-based representations of 3D vector fields defined on unstructured triangle meshes representing the boundary of complex geometries (as blood vessels are). In the present study, the numerical method for fixed points detection proposed by Bhatia (Bhatia et al. 2014) and readapted by Wang (Wang et al. 2018) was implemented because of its demonstrated numerical robustness, minimizing the risk of identification of incorrect topological structures due to numerical instabilities. The algorithm is based on the following theorem (Wang et al. 2018):

Theorem 1 *Let $\{\mathbf{x}_i, \mathbf{x}_j, \mathbf{x}_k\}$ be the vertexes of a triangle of a triangulated surface with vectors $\{\tau_i, \tau_j, \tau_k\}$, applied at the vertexes i, j, k, respectively, in a Cartesian three-dimensional reference system. There is a fixed point in the interior of the considered triangle if and only if the following determinants have all the same sign:*

$$det[\tau_i, \tau_j, \mathbf{n}], \ det[\tau_j, \tau_k, \mathbf{n}], \ det[\tau_k, \tau_i, \mathbf{n}] \tag{15}$$

where $\mathbf{n}$ is the unit vector normal to the triangle face.
Moreover, if a fixed point is located in the interior of the considered triangle, the Poincaré è index is given by:

$$Sign(det[\tau_i, \tau_j, \mathbf{n}]). \tag{16}$$

Using Theorem 1, which is related to the signed volume of a tetrahedron, fixed points of a 3D vector field can be identified. However, although the Poincar$é$ index allows to identify fixed point locations, it does not provide information about the nature of the fixed point (as summarized in Figure 3). Therefore, a criterion to distinguish between a node or a focus configuration and between an attractive or repelling nature is needed. The full classification of fixed points can be carried out using the largely adopted approach based on the analysis of the three eigenvalues $\lambda_1, \lambda_2, \lambda_3$ of the Jacobian matrix over each triangle face containing a fixed point (Gambaruto and João 2012). The eigenvalues-based fixed point classification of a 3D vector field is summarized in Table 1. In detail, in the presence of a fixed point two combinations of eigenvalues is possible, i.e., three real eigenvalues or one real eigenvalue and two complex conjugate eigenvalues. Three real eigenvalues of the same sign correspond to a node with repelling (unstable) or attracting (stable) behaviour, if the sign is positive or negative, respectively (Figure 1). A fixed point can be classified as a focus (Figure 1) in presence of complex conjugate eigenvalues (corresponding to the swirling behaviour in the plane of rotation defined by their complex eigenvectors), with their real part characterizing

Table 1 Classification of fixed points based on the eigenvalues of the linearized 3D vector field

λ	Fixed point	Poincaré index
$\lambda_1 > \lambda_2 > \lambda_3 > 0$	unstable node (source)	1
$\lambda_1 < \lambda_2 < \lambda_3 < 0$	stable node (sink)	1
$\lambda_1 < \lambda_2 < 0 < \lambda_3$	saddle point	-1
$\lambda_1 > \lambda_2 > 0 > \lambda_3$	saddle point	-1
$\lambda_1 > 0, \lambda_{2,3} = \alpha \pm \beta i$	unstable focus (source)	1
$\lambda_1 < 0, \lambda_{2,3} = -\alpha \pm \beta i$	stable focus (sink)	1

a repelling (unstable focus) or attracting (stable focus) behaviour. A fixed point can be classified as a saddle point if the three eigenvalues are real numbers but of different sign (Figure 1).

3.3 Benchmarking

An analytical 2D vector field, described by the following autonomous system:

$$\begin{cases} \dot{x} = x - \frac{x^3}{3} - y \\ \dot{y} = x - 2y, \end{cases} \tag{17}$$

is used for benchmarking and testing the proposed method. As detailed in Appendix *A*, (1) the classical method considering perturbed coordinates of the saddle point as initial condition (Arzani et al. 2017; Gambaruto and João 2012), (2) the divergence of the normalized vector field and (3) the recent trajectory-free approach (Nave and Ross 2017) is here applied to the autonomous system of eq. (17) to trace out the unstable manifold. On the same vector field, the Poincar*é* index is applied to identify fixed points.
A further analysis is performed on the luminal surface of the carotid bifurcation model. Unstable manifolds of the instantaneous WSS vector field are computed by the classical method consisting in the integration in forward time of the vector field, starting from saddle points and in the directions of the positive eigenvectors. On the same model, contraction regions are identified by negative values of the normalized WSS divergence.

3.4 WSS fixed points and manifolds analysis in patient-specific computational hemodynamics

Here, the proposed practical approach for the identification and the analysis of manifolds and fixed points of the WSS vector field at the luminal surface of an artery is applied in a two-step strategy. The two-step strategy for the analysis of the WSS fixed points is sketched in Figure 7.
    In the first step (Figure 7), the cycle-average WSS vector field at the luminal surface of both carotid bifurcation and intracranial aneurysm models:

$$\bar{\tau} = \frac{1}{T} \int_0^T \tau(t, \mathbf{x}) \, dt, \tag{18}$$
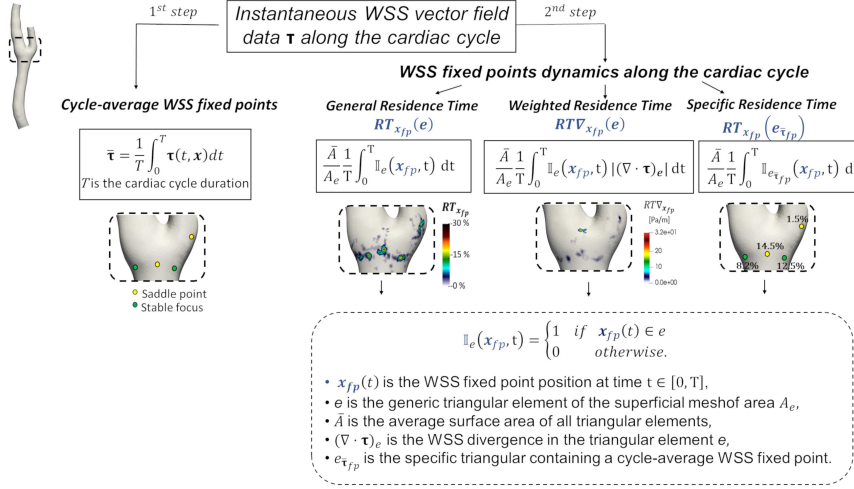
Fig. 7 Workflow of the proposed approach to WSS fixed points analysis. Fixed points are analyzed in the cycle-average WSS vector field or in the time-varying instantaneous WSS vector field. In the latter case, fixed points residence times along the cardiac cycle are calculated according to three different formulations, namely General Residence Time, Weighted Residence Time and Specific Residence Time

where T is the cardiac cycle duration, is analyzed. It has been already suggested that cycle-average WSS vector field $\bar{\tau}$ fixed points and their associated manifolds influence the near-wall intravascular transport (Arzani et al. 2016). However, it is clear from eq. (18) that it could be possible by construction that a $\bar{\tau}$ fixed point would have never been a real WSS fixed point all along the cardiac cycle (an explanatory example is presented in Appendix B). This result has stimulated a more detailed investigation, focused on the time dependence of WSS fixed points and manifolds location and nature along the cardiac cycle. Hence, as a second step of the analysis (Figure 7), here a measure of instantaneous WSS fixed points residence times along the cardiac cycle is introduced, modifying a more general formulation proposed elsewhere Arzani and Shadden (2018). In detail, the fraction of cardiac cycle (general Residence Time, RT) spent by a specific fixed point of specific nature inside a generic surface triangle is calculated as follows:

$$RT_{x_{fp}}(e) = \frac{\bar{A}}{A_e}\frac{1}{T}\int_0^T \mathbb{I}_e\left(\mathbf{x}_{fp},t\right), \qquad (19)$$

where:

$$\mathbb{I}_e\left(\mathbf{x}_{fp},t\right) = \begin{cases} 1 & \text{if } \mathbf{x}_{fp}(t) \in e \\ 0 & \text{otherwise.} \end{cases}$$

In eq. (19) $\mathbf{x}_{fp}(t)$ is the WSS fixed point position at time $t \in [0,T]$, e is the generic triangular element of the superficial mesh of area A_e and $\bar{A}$ is the average surface area of all surface triangles of the mesh characterizing the luminal surface of the vessel. Eq. (19) quantifies the fraction of cardiac cycle spent by a WSS fixed point inside the generic mesh surface element e.

Moreover, a modified version of eq. (19) is proposed here, where the residence time of a fixed point in a triangular mesh surface element is weighted by the absolute value of

the instantaneous WSS vector divergence. Physically, this weighted residence time gives a measure of the strength of the local contraction/expansion action of local shear forces:

$$RT\nabla_{x_{fp}}(e) = \frac{\bar{A}}{A_e} \frac{1}{T} \int_0^T \mathbb{I}_e\left(\mathbf{x}_{fp}, t\right) |(\nabla \cdot \tau)_e| dt, \tag{20}$$

where $(\nabla \cdot \tau)_e$ is the instantaneous WSS divergence computed in the surface triangle e containing the instantaneous WSS fixed point.

The difference between $RT_{x_{fp}}(e)$ and $RT\nabla_{x_{fp}}(e)$ resides in the term $|(\nabla \cdot \tau)_e|$, that has been incorporate into eq. (20) to measure the contraction/expansion strength acting on the wall. Roughly speaking, with respect to eq. (19), in eq. (20) the contribution of those fixed points surrounded by a marked local contraction or expansion action, even for a small fraction of the cardiac cycle, is emphasized.

Finally, in order to give a more quantitative measure to establish the physiological significance of cycle-average WSS fixed points, a measure to compute the fraction of the cardiac cycle (specific Residence Time) that the surface triangle containing a cycle-average WSS fixed point hosts an instantaneous WSS fixed point is here presented:

$$RT_{x_{fp}}\left(e_{\bar{\tau}_{fp}}\right) = \frac{\bar{A}}{A_e} \frac{1}{T} \int_0^T \mathbb{I}_{e_{\bar{\tau}_{fp}}}\left(\mathbf{x}_{fp}, t\right) dt, \tag{21}$$

where $e_{\bar{\tau}_{fp}}$ is the specific surface triangle of the superficial mesh containing a cycle-average WSS fixed point.

4 Results

4.1 Benchmarking

The results of the application of the approach proposed here to practically identify manifolds and fixed points to the autonomous system of eq. (17) confirm that the method is able to: (1) correctly approximate manifolds without resorting to the numerical integration schemes; (2) correctly identify and classify fixed points (Appendix A, Figure 15), confirming the numerical robustness of the Poincaré Index. The output of the benchmarking analysis also highlights that the proposed practical approach performs equal if not better than other trajectory-free methods. The results of testing and benchmarking are presented in Appendix A.

Finally, (1) an instantaneous map of WSS fixed points and of contraction/expansion regions, as identified by the proposed Eulerian-based practical approach at the luminal surface of the carotid bifurcation model, is presented in Figure 8, (2) superimposed to the results obtained applying the classical integration method to identify fixed points and unstable manifolds to the WSS vector field.

The results confirm that the proposed WSS divergence-based approach is a robust approximation of the WSS manifolds. In fact, WSS divergence-based contraction regions connecting WSS fixed points encase the unstable manifolds obtained through numerical integration (Figure 8).
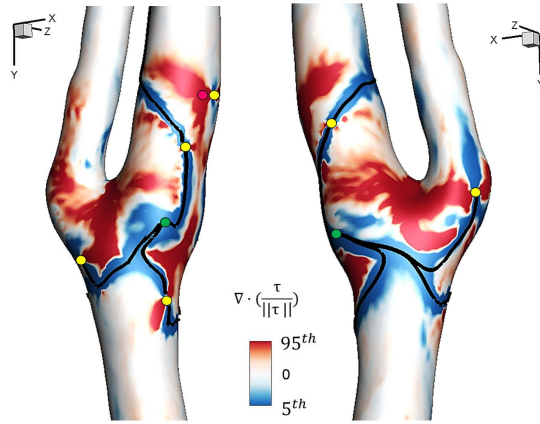
Fig. 8 Map of the identified instantaneous (the analysis refers to peak systole) WSS fixed points, of WSS divergence-based contraction regions, and WSS unstable manifolds obtained through classical numerical integration scheme at the luminal surface of the carotid bifurcation model. Unstable manifolds (black lines) start from saddle points (yellow circles) and end in stable foci (green circles). The 5th and the 95th percentile values of the $\nabla \cdot \left(\frac{\tau}{||\tau||} \right)$ distribution are set to identify contraction regions (blue color) and expansion regions (red color)

4.2 Analysis of the cycle-average WSS vector field

In this section the results obtained applying the proposed approach to realistic vascular models according to the scheme in Figure 7, are presented, and cycle-average WSS topological skeleton is analyzed.

The normalized WSS vector maps, emphasizing the structure of the vector field, allows for a clear interpretation of the results, confirming that fixed points are properly identified at the luminal surface of the carotid bifurcation (Figure 9) and of the intracranial aneurysm (Figure 10). As for the carotid bifurcation model, four saddle-type cycle-average WSS fixed points and three stable foci are identified on the luminal surface, all located at the carotid bulb. In particular, two saddle points are identified on the carotid sinus (Figure 9), one (A_C) at the outer wall of the proximal internal carotid artery (ICA), and one (D_C) at the proximal external carotid artery (ECA). The other two saddle points (C_C, E_C) and the stable foci (B_C, F_C, G_C) are identified immediately upstream of the maximum cross-sectional expansion of the carotid bulb (Figure 9). All the identified fixed points locations of the cycle-average WSS vector field belong to the bifurcation region characterized by slow, recirculating and disturbed flow that, based on the so-called hemodynamic hypothesis, promotes atherosclerosis (Morbiducci et al. 2016; Zarins et al. 1983).

Four saddle points, two stable foci and one unstable node are identified and classified at the luminal surface of intracranial aneurysm model (Figure 10). Among them, two saddle points (B_A, F_A), the two stable foci (A_A, G_A) and the unstable node (C_A) are identified on the aneurysm sac, thus reflecting the intricate aneurysmal hemodynamics. Interestingly, one stable focus is identified on the dome (A_A), consistently with previous results (Gambaruto and João 2012; Oeltze-Jafra et al. 2016). One saddle point (B_A) and the unstable node (C_A) are identified close to the neck region (Figure 10). The other two identified saddle points (D_A, E_A) are located at the luminal surface of the parent artery, in regions characterized by an intricate hemodynamics (i.e., immediately upstream of the aneurysm and close to a bi-
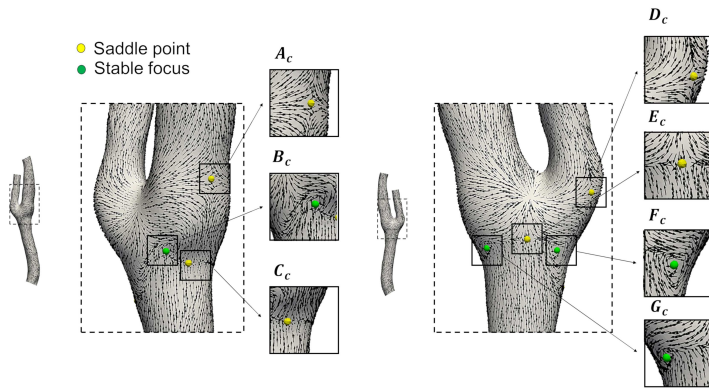
Fig. 9 Different type of cycle-average WSS fixed points in carotid bifurcation model. Vector field is normalized for visualization.Two different views and a total of 7 insets are displayed to appreciate the vector field arrangement around the fixed points. Vector field is normalized for visualization. Every third vector at the luminal surface is displayed for clarity
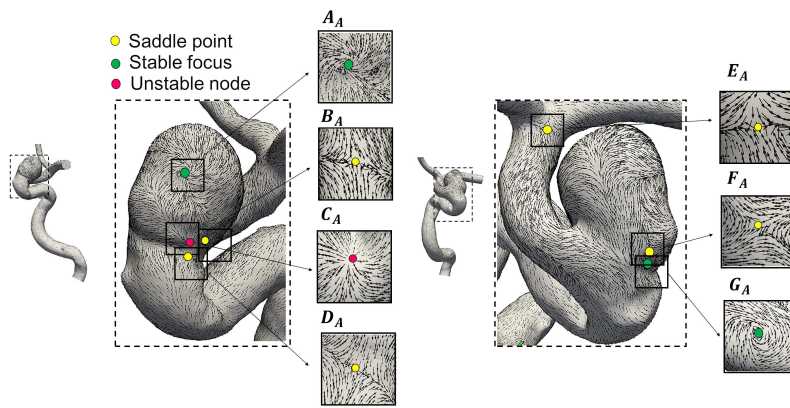
furcation, respectively).

The complete topological skeleton of the cycle-average WSS vector field at the luminal surface of carotid bifurcation and intracranial aneurysm models is presented in Figures 11 and 12, respectively. The contraction and expansion patterns, highlighted by the divergence of the normalized cycle-average WSS vector field, identify where unstable and stable manifolds are located.Moreover, the WSS divergence-based approach allows the separation of the luminal surface in regions representing the basins of attraction for the stable fixed points associated with manifolds (i.e., WSS vector trajectories starting in these areas are bound to stay in these regions, attracted to the associated stable fixed points). The effectiveness of the proposed approach in highlighting contraction/expansion regions, and partition of the luminal surface in regions with different WSS vector field behavior emerges from Figures 8, 11 and 12, and can be also appreciated considering the explanatory example presented in Figure S1, in the Online Resource. Notably, all cycle-average WSS vector stable field fixed points identified at the luminal surface of the carotid bifurcation (Figure 11) and of the intracranial aneurysm (Figure 12) are located within contraction regions, thus confirming the appropriateness of the proposed approach. On the opposite, as expected by the theory, the unstable node identified at the luminal surface of the aneurysm model, is located within an expansion region (Figure 12).

4.3 Analysis of instantaneous WSS vector field along the cardiac cycle

For an in-depth comprehension of the physiological significance of the WSS vector field fixed points, here their time of residence and nature along the cardiac cycle is investigated. In this regard, the visual inspection of the WSS field along the cardiac cycle on the luminal surface of the carotid bifurcation and intracranial aneurysm models is presented in the Online Resource through animations of the instantaneous topological skeletons of the WSS vector field throughout the cardiac cycle (carotid bifurcation: movie M1; intracranial aneurysm: movie M2).

Moreover, to further investigate the significance of the WSS fixed points and their link

Fig. 10 Different type of cycle-average WSS fixed points in intracranial aneurysm model. Vector field is normalized for visualization. Two different views and a total of 7 insets are displayed to appreciate the vector field arrangement around the fixed points. Vector field is normalized for visualization. Every third vector at the luminal surface is displayed for clarity
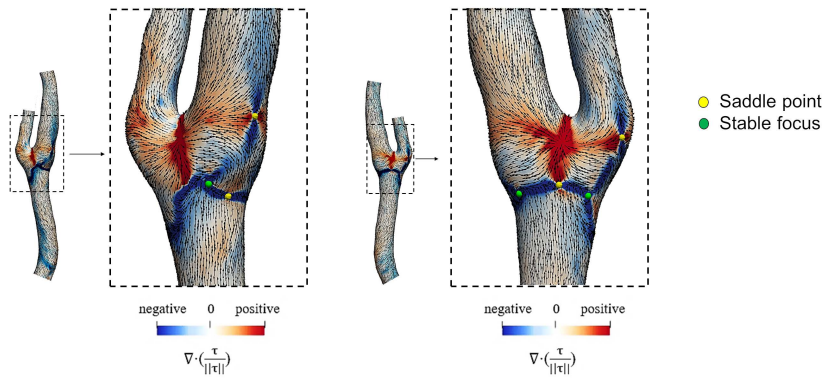
Fig. 11 Topological skeleton of cycle-average WSS vector field in carotid bifurcation model. Blue and red color define the contraction and expansion region, respectively, linking the fixed points
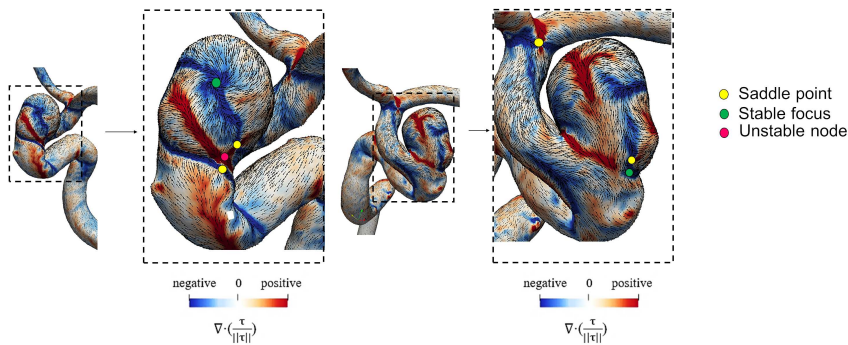
Fig. 12 Topological skeleton of cycle-average WSS vector field in intracranial aneurysm model. Blue and red color define the contraction and expansion region, respectively, linking the fixed points

with the instantaneous intravascular flow patterns in the carotid bifurcation and intracranial aneurysm, animations of vortical structures along the cardiac cycle are presented in Online Resource (carotid bifurcation: movie M3; intracranial aneurysm: movie M4), where Q-criterion has been applied. The rotating blood flow structures have been highlighted through Q isosurfaces colored by velocity magnitude.

The quantity $RT_{x_{fp}}(e)$ as defined in eq. (19) allows the evaluation of the fraction of cardiac cycle each generic surface triangle mesh element is hosting instantaneous WSS fixed points. For visualization purpose, regions of interest R_{fp} (including cycle-average WSS fixed points locations, as identified before in Figures 9, 10) are highlighted at the luminal surface around high $RT_{x_{fp}}(e)$ regions (Figures 13A,14A).

For the carotid bifurcation model, the map of $RT_{x_{fp}}(e)$ highlights that there are preferential regions at the luminal surface where instantaneous WSS saddle points and/or stable foci appear and reside for longer fraction of the cardiac cycle (Figure 13A). In detail, in regions R_{E_C} and R_{G_C} fixed points residence times is up to 30% of the cardiac cycle (Figure 13A). Overall, the presence of only-one-type instantaneous fixed points is observed in regions R_{D_C} and R_{E_C} (saddle points), and in region R_{F_C} (stable foci), while both instantaneous saddle points and stable foci are observed in regions R_{A_C}, R_{B_C}, R_{C_C}, and R_{G_C}, along the cardiac cycle (Online Resource, Figure S2). The maps of the residence times of the instantaneous type-specific observed fixed points are presented in Figure S2 in Online Resource.

Interestingly, most of the long fixed points residence time regions at the luminal surface of the carotid bifurcation fall within cycle-average low WSS regions identified by $TAWSS20$ and $TAWSS10$ maps (Figure 13A), where $TAWSS20$ ($TAWSS10$) represents the luminal surface area exposed to TAWSS below the 20th (10th) percentile. The value of 20th and 10th percentile of TAWSS are imposed according to threshold values proposed elsewhere (Gallo et al. 2018).

The quantity $RT\nabla_{x_{fp}}(e)$ defined in eq. (20) measures not only the time of residence, but also the strength of the vector field contraction/expansion around an instantaneous WSS fixed point. The luminal surface around the bifurcation apex of the carotid bifurcation model (Figure 13B) presents high $RT\nabla_{x_{fp}}(e)$ values. This is mainly the consequence of the markedly high instantaneous values of WSS divergence in that region, as also confirmed by the fact that instantaneous WSS fixed points reside for a small fraction of cardiac cycle there (Figure 13A). To complete the picture, high $RT\nabla_{x_{fp}}(e)$ spots around the apex are not located in low TAWSS regions (Figure 13). Contrarily, at locations at the bulb where fixed points reside for a longer fraction of the cardiac cycle, and where TAWSS is low (e.g., R_{E_C} and R_{G_C}, Figure 13A), $RT\nabla_{x_{fp}}(e)$ is barely lower than the apex, because of the moderate strength of the contraction/expansion of the WSS vector field, as quantified by instantaneous WSS divergence values there (Figure 13B).

Finally, a more detailed analysis carried out using the quantity $RT_{x_{fp}}\left(e_{\tau_{fp}}\right)$ as defined in eq. (21), highlights the nature and residence time of instantaneous fixed points at locations of the luminal surface where cycle-average WSS vector field fixed points were identified (see Figure 9). The results summarized in Table 2 clearly show that: (1) in general, instantaneous WSS fixed points reside for small fractions of the cardiac cycle (range $0.0 - 14.5\%$, average 6.4%) in cycle-average WSS fixed points identified locations at the luminal surface; (2) in regions R_{D_C}, R_{E_C} and R_{F_C} instantaneous WSS fixed points are of the same type as cycle-average WSS fixed points; (3) it emerges that at position C_C where a cycle-average WSS saddle point is located (Figure 9), the instantaneous WSS vector never qualifies as a fixed point along the cardiac cycle (Figure 13A), thus questioning the physical significance of WSS fixed points on cycle-average WSS vector fields; (4) weighting the time of residence

of WSS fixed points at the luminal surface with the absolute value of the WSS divergence corresponds to put more emphasis on the strength of the expansion/contraction of the WSS vector field in the closest range, which is higher in regions of the carotid bifurcation such as the apex, which are known to be scarcely atherosusceptible.

The results of the analysis of instantaneous WSS fixed points along the cardiac cycle at the luminal surface of the intracranial aneurysm model are summarized in Figure 14 and in Table 3. It can be observed that in regions R_{E_A} and R_{D_A}, identified at the luminal surface of the parent artery, the WSS fixed points residence time $RT_{x_{fp}}(e)$ reaches 70% of the cardiac cycle, meaning that instantaneous WSS fixed points spend a large fraction of the cardiac in the same position, while in regions belonging to the aneurysmal sac fixed points residence time is up to 40% of the cardiac cycle (in region R_{C_A}, Figure 14A). Contrary to what observed in the carotid bifurcation model, the presence of only-one-type of instantaneous WSS fixed point is observed in high residence time regions at the luminal surface of the aneurysm model (Table 3 and Figure S3, Online Resource). Interestingly, the long fixed points residence time locations at the luminal surface of the intracranial aneurysm model are part of the cycle-average low WSS regions identified by $TAWSS_{th}$ map, where $TAWSS_{th}$ represents the luminal surface area exposed to TAWSS below the threshold value, set according to previous studies (Jou et al. 2008) as the 10% of the value of the mean TAWSS over the parent artery (Figure 14A), the sole exception being represented by region R_{A_A} on the aneurysm dome.

In the aneurysm model, the analysis based on a combination of time of residence and strength of the WSS vector field contraction/expansion around instantaneous WSS fixed points $(RT\nabla_{x_{fp}}(e))$ highlights that: (1) high $RT\nabla_{x_{fp}}(e)$ values are located on the neck (R_{C_A} and R_{D_A}, Figure 14B), and on the dome of the aneurysmal sac (R_{A_A}, Figure 14B); (2) contrary to what observed for the carotid bifurcation, these higher $RT\nabla_{x_{fp}}(e)$ value locations on the aneurysmal neck and dome present high instantaneous values of WSS divergence and, at the same time, moderate-to-high WSS fixed points times of residence (Figure 14A); (3) $RT\nabla_{x_{fp}}(e)$ spots outside regions of interest R_{fp} identified on the aneurysmal sac are not observed; (4) at locations (R_{B_A}, R_{E_A}, R_{F_A} and R_{G_A}) where WSS fixed points reside for a sensible fraction of the cardiac cycle, (e.g., R_{E_A} Figure 14A) very low $RT\nabla_{x_{fp}}(e)$ values are observed, because of the weak contraction/expansion of the WSS vector field there.

Also in the case of the aneurysm model, the nature and residence time of instantaneous fixed points is investigated with respect to cycle-average WSS vector field fixed points (Figure 10) using the quantity $RT_{x_{fp}}\left(e_{\bar{\tau}_{fp}}\right)$.

The results of the analysis for the intracranial aneurysm are summarized in Table 3, from which emerges that: (1) instantaneous WSS fixed points reside for large fractions of the cardiac cycle (58.2% and 46.2%) in cycle-average WSS fixed points locations at the luminal surface of the parent vessel; (2) considering cycle-average WSS fixed points on the aneurysmal sac (A_A, B_A, C_A, F_A, G_A, Figures 10 and 14A), instantaneous WSS fixed points reside at those locations for moderate fractions of the cardiac cycle (range $3.6-21.3\%$, average 11.4%); (3) the instantaneous WSS fixed points are always of the same nature as cycle-average WSS fixed points; (4) at position A_A where a cycle-average WSS stable focus is identified (Figure 10), the instantaneous WSS vector qualifies always as a stable focus for the 10.3% of the cardiac cycle (Table 3), but this location does not fall within cycle-average low WSS regions identified by $TAWSS_{th}$ map, thus questioning again the physical significance of WSS fixed points on cycle-average WSS vector fields; (5) elevated values of the strength of the expansion/contraction of the WSS vector field around instantaneous WSS
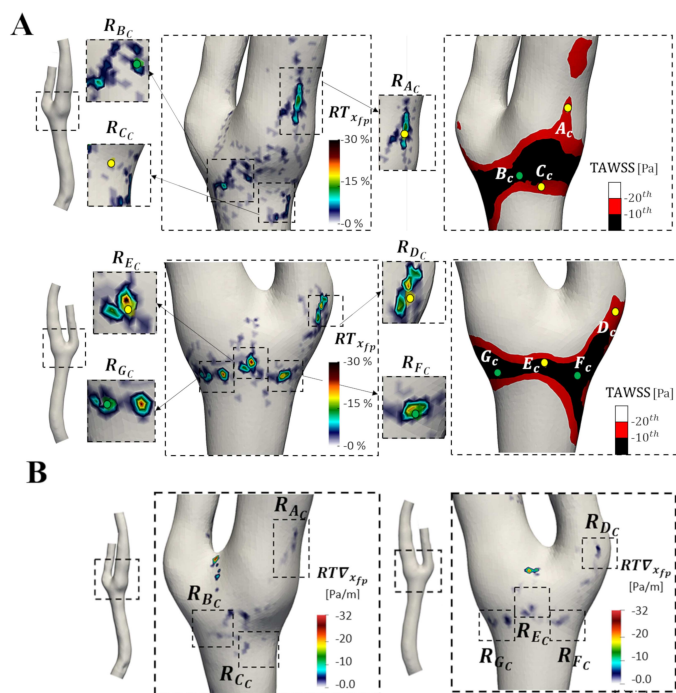
Fig. 13 Panel A: Map of fixed points residence time $RT_{x_{fp}}(e)$ on the carotid bifurcation model. Two views and seven insets are displayed, zooming on the locations of cycle-average WSS fixed points. Yellow points denote the presence of a saddle point, while green points indicate a stable focus. In the right panels, the exposure to low TAWSS is visualized. Red and black areas denote TAWSS values below respectively the 20th and 10th percentile of the TAWSS distribution. Panel B: Map of measure $RT\nabla_{x_{fp}}(e)$ on the carotid bifurcation model. Two views are displayed. Dashed lines delimit regions $R_{A_C}, R_{B_C}, R_{C_C}, R_{D_C}, R_{E_C}, R_{F_C}$, and R_{G_C}

fixed points are observed on the aneurysmal dome and close to the neck region, reflecting the intricate hemodynamics characterizing these regions.

5 Discussion

The here presented practical approach for the topological skeleton analysis of WSS at the vessel luminal surface is intended as a contribution to further investigate the still debated role of WSS in vascular physiopathology (Gallo et al. 2018; Liang et al. 2019) . More specifically, the WSS topological skeleton highlights blood flow features typically associated with atherosclerosis initiation, as (1) a WSS fixed point is by definition a focal point where the WSS vector is null, and (2) unstable/stable WSS manifolds, quantifying the strength of contraction/expansion around the fixed point, are associated to near wall flow separation and reversal (Arzani and Shadden 2018). These blood flow features have been previously reported to favor atherosclerosis initiation in the carotid bifurcation (Morbiducci et al. 2016). Moreover, the WSS topological skeleton also highlights blood flow features which are relevant for the study of cerebral aneurysm. In detail, WSS fixed points and manifolds can highlight the

Table 2 Analysis of WSS fixed points residence time and nature along the cardiac cycle on the carotid bifurcation model. $TAWSS20$ ($TAWSS10$) represents the luminal surface area exposed to TAWSS below the 20th (10th) percentile. SPs and SFs denote Saddle Points and Stable Foci, respectively

Region of interest R_{fp}	Instantaneous WSS fixed points nature in R_{fp}	Cycle-Average WSS fixed point nature in R_{fp}	Instantaneous WSS residence time fixed points and nature at cycle-average WSS fixed point location in R_{fp}	WSS fixed points residence time and the local contraction/expansion in R_{fp}	TAWSS percentile at cycle-average WSS fixed point location in R_{fp}
R_{A_C}	SPs and SFs	SP (A_C)	3.4% (3.4% SPs, 0% SFs)	Low values of $RT\nabla_{x_{fp}}$	$TAWSS20$
R_{B_C}	SPs and SFs	SF (B_C)	4.9% (2% SPs, 2.9% SFs)	Low values of $RT\nabla_{x_{fp}}$	$TAWSS10$
R_{C_C}	SPs and SFs	SP (C_C)	0% (0% SPs, 0% SFs)	Low values of $RT\nabla_{x_{fp}}$	$TAWSS20$
R_{D_C}	SPs	SP (D_C)	1.5% (1.5% SPs, 0% SFs)	Low values of $RT\nabla_{x_{fp}}$	$TAWSS20$
R_{E_C}	SPs	SP (E_C)	14.5% (14.5% SPs, 0% SFs)	Low values of $RT\nabla_{x_{fp}}$	$TAWSS10$
R_{F_C}	SFs	SF (F_C)	12.5% (0% SPs, 12.5% SFs)	Low values of $RT\nabla_{x_{fp}}$	$TAWSS10$
R_{G_C}	SPs and SFs	SF (G_C)	8.2% (0% SPs, 8.2% SFs)	Low values of $RT\nabla_{x_{fp}}$	$TAWSS10$
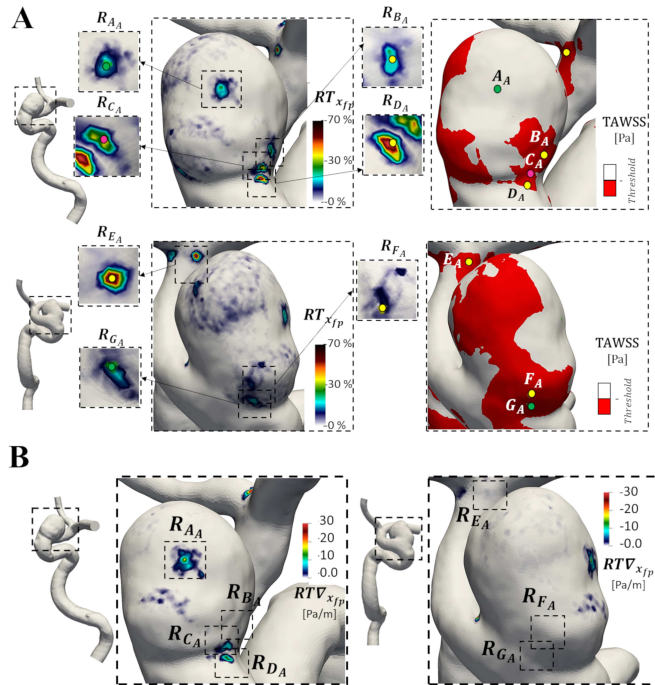
Fig. 14 Panel A: Map of fixed points residence time $RT_{x_{fp}}$ (e) on the intracranial aneurysm model. Two views and seven insets are displayed, zooming on the locations of cycle-average WSS fixed points. Yellow points denote the presence of a saddle point, green points indicate a stable focus, red points indicate unstable nodes. In the right panels, the exposure to low TAWSS is visualized. Red area denotes TAWSS values below the fixed threshold (10% of the value of the mean TAWSS over the parent artery). Panel B: Map of measure $RT\nabla_{x_{fp}}$ (e) on the intracranial aneurysm model. Two views are displayed. Dashed lines delimit regions R_{A_A}, R_{B_A}, R_{C_A}, R_{D_A}, R_{E_A}, R_{F_A}, and R_{G_A}

**Table 3** Analysis of WSS fixed points residence time and nature along the cardiac cycle on the intracranial aneurysm model. $TAWSS_{th}$ represents the luminal surface area exposed to TAWSS below the 10% of the value of the mean TAWSS over the parent artery. SPs, SFs and UNs denote Saddle Points, Stable Foci and Unstable Nodes, respectively

Region of interest R_{fp}	Instantaneous WSS fixed points nature in R_{fp}	Cycle-Average WSS fixed point nature in R_{fp}	Instantaneous WSS residence time fixed points and nature at cycle-average WSS fixed point location in R_{fp}	WSS fixed points residence time and the local contraction/expansion in R_{fp}	TAWSS percentile at cycle-average WSS fixed point location in R_{fp}
R_{A_A}	SFs	SF (A_A)	10.3% SFs	High values of $RT\nabla_{x_{fp}}$	
R_{B_A}	SPs	SP (B_A)	15.3% SPs	Very low values of $RT\nabla_{x_{fp}}$	$TAWSS_{th}$
R_{C_A}	UNs	UN (C_A)	21.3% UNs	Moderate values of $RT\nabla_{x_{fp}}$	$TAWSS_{th}$
R_{D_A}	SPs	SP (D_A)	46.2% SPs	Moderate values of $RT\nabla_{x_{fp}}$	$TAWSS_{th}$
R_{E_A}	SPs	SP (E_A)	58.2% SPs	Very lowvalues of $RT\nabla_{x_{fp}}$	$TAWSS_{th}$
R_{F_A}	SPs	SP (F_A)	3.6% SPs	Very low values of $RT\nabla_{x_{fp}}$	$TAWSS_{th}$
R_{G_A}	SFs	SF (G_A)	6.6% SFs	Very low values of $RT\nabla_{x_{fp}}$	$TAWSS_{th}$

area of flow impingement at the aneurysm wall, and generally the area where vortex structures interact with the wall (Goodarzi Ardakani et al. 2019; Yagi et al. 2013). These fluid mechanics features have been previously associated to aneurysm formation, remodeling, and rupture (Cebral et al. 2005). Indirect evidences on the link between WSS topological skeleton and vascular dysfunction are provided by studies documenting a focal response of endothelial cells (ECs) to both low WSS magnitude (and a WSS fixed point is by definition a location where ECs experience a null WSS value) and marked directional changes. Furthermore, recent studies highlighted that the WSS topological skeleton is strongly linked to arterial near-wall mass transport and could explain luminal surface concentration patterns of, e.g., low density lipoprotein or oxygen (Arzani and Shadden 2016; Arzani et al. 2017), which are involved in the atherosclerosis initiation processes. The emerged link of the WSS topological skeleton with the near-wall flow features (responsible for shaping, e.g., LDL and oxygen concentrations), in association with the WSS contraction/expansion action onto the luminal surface (responsible for mechanically-induced changes in endothelium permeability (Tarbell 2010)) highlighted by the WSS manifolds, could influence blood-vessel mass transfer.

5.1 Comparison with previous studies

Previous studies addressing the WSS topological skeleton analysis are mostly based on Lagrangian approaches (Arzani and Shadden 2016; Arzani et al. 2017). Among them, WSS Lagrangian coherent structures have been demonstrated to match the manifolds of the cycle-average WSS vector field (Arzani and Shadden 2016). Although such Lagrangian-based approach enables the detection of time-dependent topological structures in complex flows, it requires a high number of Lagrangian tracers to be seeded and generally a high computation effort (Reza and Arzani 2019). Therefore, a direct and practical Eulerian method to capture WSS manifolds, avoiding the numerical integration required for Lagrangian-based technique, reduces the computational cost. Recently, a new trajectory-free method approximate phase space manifolds was proposed and applied on a 2D analytical vector field (Nave

and Ross 2017). Such method is based on the computation of the trajectory divergence rate, i.e. the rate at which the normal distance between nearby trajectories grows at every position in the domain of the vector field. Although this method proves that a Eulerian-based approach may be used to approximate manifolds, its extension to 3D vector field on complex geometries is not trivial and computationally expensive, as it requires the computation of the normal, tangent and binormal plane to a trajectory at every point in the domain.

Stimulated from this context, the here proposed Eulerian-based approach to WSS topological skeleton identification on 3D complex vascular geometries has the potential of simplifying and speeding up studies on the physiological significance of WSS topological skeleton in cardiovascular flows. In detail, (1) based on Volume Contraction Theory, WSS stable/unstable manifolds on the luminal surface of vessels are traced out using the divergence of the normalized WSS vector field, which highlights shear local expansion/contraction, and (2) based on Poincaré index and Jacobian analysis, WSS fixed points can be identified on 3D complex surfaces. The proposed approach was tested on an analytical 2D vector field, providing excellent results.

The here presented approach is considered practical as it can be easily implemented: it requires only the WSS vector field as output from the CFD simulation, and the post-processing algorithms, based on a robust theory, are easy to be reproduced. It should be noted that alternatively the WSS divergence can be easily computed using largely adopted open-source codes (e.g., ParaView and VMTK), as well as commercial codes. This approach significantly reduces computational costs, since there is no need for Lagrangian surface transport computation and for numerical integration schemes assuring high-order accuracy, as required for Lagrangian-based and integrated trajectory-based methods, respectively (Gambaruto and João 2012; Reza and Arzani 2019). Furthermore, it is physically intuitive and does not require a high level of experience. Finally, the proposed approach is characterized by modularity, in the sense that most of the steps indicated in Figure 3 are independent and therefore can be adopted separately (e.g., only for the purpose of fixed points identification and/or classification, or only for manifolds), or used in combination with other approaches.

5.2 Analysis of the unsteady nature of WSS fixed points

Unlike previous studies focusing on the cycle-average WSS topological skeleton (Arzani and Shadden 2016; Arzani et al. 2017), here the Eulerian-based practical approach has allowed to easily analyze the unsteady nature of WSS fixed points along the cardiac cycle. In general, it emerged that WSS fixed points patterns is markedly instantaneous by nature, with fixed points appearing, moving, disappearing and changing their nature at predisposed locations at the luminal surface of a vessel, along the cardiac cycle. More in detail, on the carotid bifurcation model, it was observed that (1) most of the instantaneous WSS fixed points reside in low cycle-average WSS regions (Figure 13A); (2) expansion/contraction of the WSS vector field is strong around those fixed points located in the bifurcation apex, a scarcely atherosusceptible region (Figure 13B); (3) instantaneous WSS fixed points co-localize with cycle-average WSS fixed points for small fractions of the cardiac cycle (Table 2); (4) instantaneous WSS fixed points move along the luminal surface in regions characterized by slow, recirculating and disturbed flow (movie M1, Online Resource); (5) a persistent saddle point and its associated unstable manifold is present on the outer wall of the ICA, as a consequence of the two counter-rotating blood flow structures developing in the ICA (movie M3, Online Resource).

As for the intracranial aneurysm model, it emerged that: (1) both the aneurysmal dome and

the neck region are characterized by a marked WSS expansion/contraction action (Figure 14B); (2) an instantaneous focus is present on the aneurysm dome throughout the cardiac cycle (movie M2, Online Resource), as a consequence of the interaction with the wall of the dynamic vortex structures developing in the sac (Figure 14A and movie M4, Online Resource); (3) instantaneous WSS fixed points co-localize with cycle-average WSS fixed points locations for moderate fractions of the cardiac cycle on the aneurysmal sac, and for large fractions on the parent vessel (Table 3). Furthermore, the present analysis highlights the importance of considering the unsteadiness of WSS fixed points and manifolds along the cardiac cycle. The consideration of WSS fixed points analysis along the cardiac cycle enriches the information that can be obtained when considering cycle-average WSS topological skeleton (Arzani and Shadden 2016; 2018; Arzani et al. 2017): with respect to previous studies mainly focusing on cycle-average WSS topological skeleton, the present findings underline the physical significance of WSS fixed points dynamics along the cardiac cycle. More in detail, it emerged that: (1) on the carotid bifurcation model, the location on the luminal surface where a cycle-average WSS saddle point is located never hosts instantaneous WSS fixed points along the cardiac cycle (Table 2); (2) on the intracranial aneurysm model, a persistent instantaneous WSS focus moves over a confined surface area of the sac which is not co-localized with the cycle-average low WSS region (Table 3). In addition, a quantity is proposed here to analyze the dynamic nature of the WSS fixed points (eq. (20)) by weighting the time of residence of WSS fixed points with the absolute value of the algebraic summation of the three eigenvalues in eq. (6), (corresponding to absolute value of the WSS divergence). This differs from the sum of the absolute values of the single eigenvalue proposed elsewhere (Arzani and Shadden 2018). The rationale for the implemented weighting strategy lies in the physical meaning of the absolute value of WSS divergence, representing the strength of the contraction/expansion of the WSS vector field around the fixed point.

5.3 Limitations of the study

As a first limitation, the exact mechanisms by which the WSS topological skeleton and related descriptors influence vascular biology are still underexplored, therefore biological mechanism studies, prospective studies or longitudinal data are warranted and encouraged. Although our practical approach allows the characterization of the unsteadiness of WSS fixed points along the cardiac cycle, at this stage of the investigation it does not provide information about their kinematics, as it does not track automatically the location of each fixed point along the cardiac cycle (which is typical of Lagrangian-based approaches). However, in future studies a method for analyzing WSS fixed points kinematics based upon the here presented approach will be developed, allowing to reconstruct single fixed points paths over the luminal surface along the cardiac cycle.

Moreover, the impact of the resolution of CFD data on the fidelity of fixed points analysis remains to be determined. In this study, the affordable computational cost of the proposed method allowed the use of fine resolution CFD data.

5.4 Conclusions

In conclusion, the here presented study represents the theoretical and methodological basis aiming at (1) speeding up studies on the physiological significance of WSS topological skeleton in cardiovascular flows, (2) increasing the number of evidence about the role of

WSS topological features in vascular pathophysiology, in the context of the increasing interest as expressed by recent literature on this still underexplored topic. The findings of this analysis aim at facilitating the assessment of topological features, ultimately increasing the chance of finding mechanistic explanations to clinical observations. Future studies detailing how WSS fixed points and WSS vector field contraction/expansion impact vascular mechanobiology are warranted and encouraged.

References

Andersson M, Lantz J, Ebbers T, Karlsson M (2017) Multidirectional WSS disturbances in stenotic turbulent flows: A pre- and post-intervention study in an aortic coarctation. J Biomech 51:8–16, DOI 10.1016/j.jbiomech.2016.11.064, URL http://dx.doi.org/10.1016/j.jbiomech.2016.11.064

Argyris JH, Faust G, Haase M, Friedrich R (2015) An Exploration of Dynamical Systems and Chaos. DOI 10.1007/978-3-662-46042-9

Arzani A, Shadden SC (2016) Characterizations and Correlations of Wall Shear Stress in Aneurysmal Flow. J Biomech Eng 138(1), DOI 10.1115/1.4032056

Arzani A, Shadden SC (2018) Wall shear stress fixed points in cardiovascular fluid mechanics. J Biomech 73:145–152, DOI 10.1016/j.jbiomech.2018.03.034, URL https://doi.org/10.1016/j.jbiomech.2018.03.034

Arzani A, Gambaruto AM, Chen G, Shadden SC (2016) Lagrangian wall shear stress structures and near-wall transport in high-Schmidt-number aneurysmal flows. J Fluid Mech 790:158–172, DOI 10.1017/jfm.2016.6

Arzani A, Gambaruto AM, Chen G, Shadden SC (2017) Wall shear stress exposure time: a Lagrangian measure of near-wall stagnation and concentration in cardiovascular flows. Biomech Model Mechanobiol 16(3):787–803, DOI 10.1007/s10237-016-0853-7

Baek H, Jayaraman MV, Richardson PD, Karniadakis GE (2010) Flow instability and wall shear stress variation in intracranial aneurysms. J R Soc Interface 7(47):967–988, DOI 10.1098/rsif.2009.0476

Bhatia H, Gyulassy A, Wang H, Bremer Pt, Pascucci V (2014) Topological Methods in Data Analysis and Visualization III pp 3–18, DOI 10.1007/978-3-319-04099-8, URL http://link.springer.com/10.1007/978-3-319-04099-8

Cebral JR, Castro MA, Burgess JE, Pergolizzi RS, Sheridan MJ, Putman CM (2005) Characterization of Cerebral Aneurysms for Assessing Risk of Rupture By Using Patient-Specific Computational Hemodynamics Models. Am J Neuroradiol 26(10):2550 LP – 2559, URL http://www.ajnr.org/content/26/10/2550.abstract

Chien A, Tateshima S, Castro M, Sayre J, Cebral J, Vinuela F (2008) Patient-specific flow analysis of brain aneurysms at a single location: comparison of hemodynamic characteristics in small aneurysms. Med Biol Eng Comput 46(11):1113–1120, DOI 10.1007/s11517-008-0400-5

Chnafa C, Bouillot P, Brina O, Najafi M, Delattre BMA, Vargas MI, Pereira VM, Steinman DA (2018) Errors in power-law estimations of inflow rates for intracranial aneurysm CFD. J Biomech 80:159–165, DOI 10.1016/j.jbiomech.2018.09.006, URL http://www.ncbi.nlm.nih.gov/pubmed/30243498

Chung B, Cebral JR (2015) CFD for evaluation and treatment planning of aneurysms: review of proposed clinical uses and their challenges. Ann Biomed Eng 43(1):122–138, DOI 10.1007/s10439-014-1093-6

Ethier C, Prakash S, A Steinman D, Leask R, G Couch G, Ojha M (2000) Steady flow separation patterns in a 45 degree junction. J Fluid Mech (2000), 411, pp 1-38 411, DOI 10.1017/S0022112099008022

Ethier CR (2002) Computational modeling of mass transfer and links to atherosclerosis. Ann Biomed Eng 30(4):461–471

Fatehi Hassanabad A, Garcia J, Verma S, White JA, Fedak PWM (2019) Utilizing wall shear stress as a clinical biomarker for bicuspid valve-associated aortopathy. Curr Opin Cardiol 34(2):124–131, DOI 10.1097/HCO.0000000000000601

Gallo D, Steinman DA, Morbiducci U (2015) An insight into the mechanistic role of the common carotid artery on the hemodynamics at the carotid bifurcation. Ann Biomed Eng 43(1):68–81, DOI 10.1007/s10439-014-1119-0

Gallo D, Steinman DA, Morbiducci U (2016) Insights into the co-localization of magnitude-based versus direction-based indicators of disturbed shear at the carotid bifurcation. J Biomech 49(12):2413–2419, DOI 10.1016/j.jbiomech.2016.02.010

Gallo D, Bijari PB, Morbiducci U, Qiao Y, Xie YJ, Etesami M, Habets D, Lakatta EG, Wasserman BA, Steinman DA (2018) Segment-specific associations between local haemodynamic and imaging markers of early atherosclerosis at the carotid artery: an in vivo human study. J R Soc Interface 15(147), DOI 10.1098/rsif.2018.0352

Gambaruto AM, João AJ (2012) Computers & Fluids Flow structures in cerebral aneurysms. Comput Fluids 65:56–65, DOI 10.1016/j.compfluid.2012.02.020, URL http://dx.doi.org/10.1016/j.compfluid.2012.02.020

Gambaruto AM, Doorly DJ, Yamaguchi T (2010) Wall shear stress and near-wall convective transport: Comparisons with vascular remodelling in a peripheral graft anastomosis. J Comput Phys 229(14):5339–5356, DOI 10.1016/j.jcp.2010.03.029, URL http://dx.doi.org/10.1016/j.jcp.2010.03.029

Ge L, Sotiropoulos F (2010) Direction and magnitude of blood flow shear stresses on the leaflets of aortic valves: is there a link with valve calcification? J Biomech Eng 132(1):14505, DOI 10.1115/1.4000162

Goodarzi Ardakani V, Tu X, Gambaruto AM, Velho I, Tiago J, Sequeira A, Pereira R (2019) Near-Wall Flow in Cerebral Aneurysms. Fluids 4(2):89, DOI 10.3390/fluids4020089, URL https://www.mdpi.com/2311-5521/4/2/89

Goubergrits L, Thamsen B, Berthe A, Poethke J, Kertzscher U, Affeld K, Petz C, Hege HC, Hoch H, Spuler A (2010) In vitro study of near-wall flow in a cerebral aneurysm model with and without coils. AJNR Am J Neuroradiol 31(8):1521–1528, DOI 10.3174/ajnr.A2121

Goubergrits L, Schaller J, Kertzscher U, Van Den Bruck N, Poethkow K, Petz C, Hege HC, Spuler A (2012) Statistical wall shear stress maps of ruptured and unruptured middle cerebral artery aneurysms. J R Soc Interface 9(69):677–688, DOI 10.1098/rsif.2011.0490

He X, Ku DN (1996) Pulsatile flow in the human left coronary artery bifurcation: average conditions. J Biomech Eng 118(1):74–82

Hoi Y, Wasserman BA, Lakatta EG, Steinman DA (2010) Effect of common carotid artery inlet length on normal carotid bifurcation hemodynamics. J Biomech Eng 132(12):121008, DOI 10.1115/1.4002800

Jou LD, Lee DH, Morsi H, Mawad ME (2008) Wall shear stress on ruptured and unruptured intracranial aneurysms at the internal carotid artery. Am J Neuroradiol 29(9):1761–1767, DOI 10.3174/ajnr.A1180

Kallmes DF (2012) Point: CFD–computational fluid dynamics or confounding factor dissemination. DOI 10.3174/ajnr.A2993

Lévêque A (1928) Les Lois de la Transmission de Chaleur Par Convection. Ann Mines 13

Liang L, Steinman DA, Brina O, Chnafa C, Cancelliere NM, Pereira VM (2019) Towards the Clinical utility of CFD for assessment of intracranial aneurysm rupture - a systematic review and novel parameter-ranking tool. J Neurointerv Surg 11(2):153–158, DOI 10.1136/neurintsurg-2018-014246

Malek AM, Alper SL, Izumo S (1999) Hemodynamic shear stress and its role in atherosclerosis. JAMA 282(21):2035–2042

Minev P, Ross Ethier C (1999) A characteristic/finite element algorithm for the 3-D Navier–Stokes equations using unstructured grids. Comput Methods Appl Mech Eng 178(1-2):39–50, DOI 10.1016/s0045-7825(99)00003-1

Morbiducci U, Gallo D, Cristofanelli S, Ponzini R, Deriu MA, Rizzo G, Steinman DA (2015) A rational approach to defining principal axes of multidirectional wall shear stress in realistic vascular geometries, with application to the study of the influence of helical flow on wall shear stress directionality in aorta. J Biomech 48(6):899–906, DOI 10.1016/j.jbiomech.2015.02.027

Morbiducci U, Kok AM, Kwak BR, Stone PH, Steinman DA, Wentzel JJ (2016) Atherosclerosis at arterial bifurcations: Evidence for the role of haemodynamics and geometry. Thromb Haemost 115(3):484–492, DOI 10.1160/TH15-07-0597

Mortensen M, Valen-Sendstad K (2015) Oasis: A high-level/high-performance open source Navier–Stokes solver. Comput Phys Commun 188, DOI 10.1016/j.cpc.2014.10.026

Nave GK, Ross SD (2017) Trajectory-free calculation of attracting and repelling manifolds (August), URL http://arxiv.org/abs/1705.07949, 1705.07949

Oeltze-Jafra S, Cebral JR, Janiga G, Preim B (2016) Cluster Analysis of Vortical Flow in Simulations of Cerebral Aneurysm Hemodynamics. IEEE Trans Vis Comput Graph 22(1):757–766, DOI 10.1109/TVCG.2015.2467203

Peiffer V, Sherwin SJ, Weinberg PD (2013a) Computation in the rabbit aorta of a new metric - the transverse wall shear stress - to quantify the multidirectional character of disturbed blood flow. J Biomech 46(15):2651–2658, DOI 10.1016/j.jbiomech.2013.08.003

Peiffer V, Sherwin SJ, Weinberg PD (2013b) Does low and oscillatory wall shear stress correlate spatially with early atherosclerosis? A systematic review. Cardiovasc Res 99(2):242–250, DOI 10.1093/cvr/cvt044

Reza MMS, Arzani A (2019) A critical comparison of different residence time measures in aneurysms. J Biomech DOI 10.1016/j.jbiomech.2019.03.028

Shadden SC, Arzani A (2015) Lagrangian postprocessing of computational hemodynamics. Ann Biomed Eng 43(1):41–58, DOI 10.1007/s10439-014-1070-0

Suzuki D, Funamoto K, Sugiyama S, Nakayama T, Hayase T, Tominaga T (2015) Investigation of characteristic hemodynamic parameters indicating thinning and thickening sites of cerebral aneurysms. J Biomech Sci Eng 10(1):1–10, DOI 10.1299/jbse.14-00265

Tarbell JM (2010) Shear stress and the endothelial transport barrier. Cardiovasc Res 87(2):320–330, DOI 10.1093/cvr/cvq146

Tobe Y, Yagi T, Iwabuchi Y, Yamanashi M, Takamura K, Sugiura T, Umezu M, Hayashi Y, Yoshida H, Nakajima A, Nishitani K, Okada Y, Sugawara M, Hiraguchi S, Kubo T, Kitahara S (2014) Relationship between Pathology and Hemodynamics of Human Unruptured Cerebral Aneurysms. In: Goh J (ed) 15th Int. Conf. Biomed. Eng., Springer International Publishing, Cham, pp 44–47

Tricoche X, Wischgoll T, Scheuermann G, Hagen H (2002) Topology tracking for the visualization of time-dependent two-dimensional flows. Comput Graph 26(2):249–257, DOI 10.1016/S0097-8493(02)00056-0

Valen-Sendstad K, Steinman DA (2014) Mind the gap: impact of computational fluid dynamics solution strategy on prediction of intracranial aneurysm hemodynamics and rup-

ture status indicators. AJNR Am J Neuroradiol 35(3):536–543, DOI 10.3174/ajnr.A3793

Wang W, Wang W, Li S (2018) Detection and classification of critical points in piecewise linear vector fields. J Vis 21(1):147–161, DOI 10.1007/s12650-017-0438-2, URL https://doi.org/10.1007/s12650-017-0438-2

Yagi T, Sato A, Shinke M, Takahashi S, Tobe Y, Takao H, Murayama Y, Umezu M (2013) Experimental insights into flow impingement in cerebral aneurysm by stereoscopic particle image velocimetry: transition from a laminar regime. J R Soc Interface 10(82):20121031, DOI 10.1098/rsif.2012.1031

Zarins CK, Giddens DP, Bharadvaj BK, Sottiurai VS, Mabon RF, Glagov S (1983) Carotid bifurcation atherosclerosis. Quantitative correlation of plaque localization with flow velocity profiles and wall shear stress. Circ Res 53(4):502–514

Appendix A Benchmarking

The analytical 2D vector field described by eq. (17) and used here for benchmarking is characterized by the presence of a saddle point configuration in the origin of the cartesian reference system, and two symmetrical stable foci at cartesian coordinates $\left(\pm 2\sqrt{\frac{3}{8}}; \pm\sqrt{\frac{3}{8}}\right)$.

To trace out the unstable manifold, the classical method was applied considering perturbed coordinates of the saddle point as initial condition (Arzani et al. 2017; Gambaruto and João 2012). The numerical integration was carried out by applying the *Runge Kutta Fehlberg* $4-5$ numerical scheme and integration was continued until the trajectory reached the other fixed point. On the same vector field (1) the divergence of normalized vector field was computed to identify contraction/expansion regions and (2) the Poincaré index was used to identify fixed points. For an in-depth benchmarking, the recent trajectory-free method proposed by (Nave and Ross 2017) was here applied on the autonomous system of eq. (17) to find attracting and repelling invariant manifolds using the trajectory divergence rate $\dot{\rho}$ defined by:

$$\dot{\rho} = \mathbf{n}^T \mathbf{S}\, \mathbf{n}, \tag{22}$$

where $\mathbf{n}$ is the unit vector normal and S the rate-of-strain tensor. The autonomous system of eq. (17) is presented in Figure 15, where the position of the three fixed points is highlighted and the unstable manifold (corresponding to a saddle-type fixed point and calculated according to (Arzani et al. 2017; Gambaruto and João 2012), is delineated. It can be observed that the map of the divergence of the normalized vector field perfectly encases the unstable manifold within the contraction region (blue color in Figure 15, panel B) according to theory: regions of negative divergence correspond to converging vectors and unstable manifolds tend to attract nearby trajectories (the distance between points belonging to unstable manifolds decreases producing a converging point series).

Finally, the results obtained implementing the trajectory-free method proposed elsewhere (Nave and Ross 2017) on the autonomous system of eq. (17), reported in Figure 15 panel C, clearly show that the divergence of normalized vector map captured the unstable manifold of the system as well as the trajectory divergence rate $\dot{\rho}$. Notably, although both the divergence-based methods provide a scalar measure to quantify the attraction/repulsion of nearby trajectories, the here proposed divergence of the normalized vector field captured the unstable manifold only, as opposed to the trajectory divergence rate $\dot{\rho}$, that highlighted also regions of the phase space that are not an unstable manifold (Figure 15, panel C).
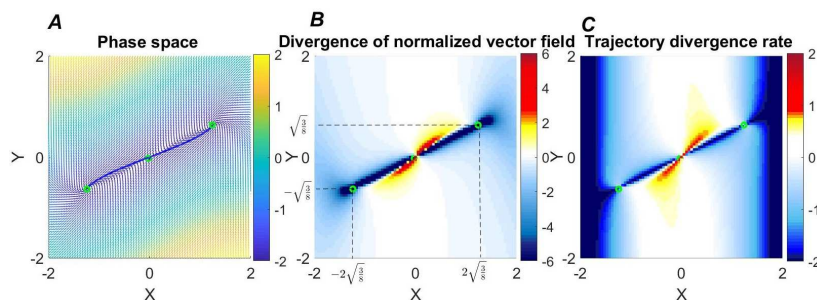
Fig. 15 Panel A: Fixed points (green circles) and attractive manifold (blue line). Vector field is normalized for visualization and colored based on its magnitude. Panel B: Divergence of the normalized vector field. Panel C: Trajectory divergence rate field

Appendix B   About the physiological significance of the cycle-average WSS vector fixed points

A cycle-average WSS vector field ($\bar{\tau}$) fixed point would have never been a null vector along the cardiac cycle, i.e., it would have never been a real fixed point. This is also confirmed by the explanatory example in Figure 16, where it is shown that the fact that $\bar{\tau} = 0$ at a point at the luminal surface of the vessel does not necessarily implies that at the same point the Time-Averaged Wall Shear Stress (TAWSS), i.e., the cycle average value of the magnitude of vector $\tau(t, \mathbf{x})$, is null. In fact, from the Integral Inequality Absolute Value it follows that:

$$|\bar{\tau}(\mathbf{x})| = |\frac{1}{T}\int_0^T \tau(t,\mathbf{x})dt| \leqslant \frac{1}{T}\int_0^T |\tau(t,\mathbf{x})|dt = \text{TAWSS}(\mathbf{x}), \qquad (23)$$

suggesting that a null value for $|\bar{\tau}|$ does not necessarily imply the same for TAWSS. Moreover, it can be easily demonstrated that:

$$\text{TAWSS}(\mathbf{x}) = 0 \;\leftrightarrow\; |\tau(t,\mathbf{x})| = 0 \;\forall t \in [0,T], \qquad (24)$$

since $|\tau(t,\mathbf{x})|$ is a non-negative function $\forall t \in [0,T]$. Eqns 23 and 24 call into question the real physical meaning of fixed points of the cycle-average WSS vector field at the luminal surface. In particular, eq. (24) clearly states that a fixed point of the cycle-average WSS vector field at a specific location at the luminal surface is a real fixed point if and only if the WSS vector at that location is always a fixed point (i.e., is always a null vector), along the cardiac cycle. The intricate near-wall and intravascular hemodynamics establishing in most healthy and diseased vessels make this a rarely satisfied condition in the arterial system. Notably, in the presence of a real, physically meaningful fixed point of the cycle-average WSS vector field as the one identified by the condition of eq. (24), the definition of other WSS-based descriptors measuring WSS directionality such as the Oscillatory Shear Index (OSI) (He and Ku 1996), and the transverse Wall Shear Stress (transWSS) (Peiffer et al. 2013a) become meaningless. In light of this, a practical method for an in-depth analysis of the instantaneous WSS fixed points along the cardiac cycle is needed.

Appendix C   Online Resource

Supplementary materials associated with this article can be found in the online version.
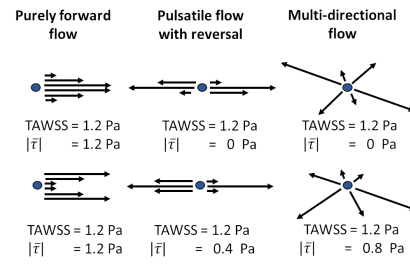
Fig. 16 Comparison between $|\bar{\tau}|$ and TAWSS in three different flow environments at the luminal surface of an artery. The black arrows depict WSS vectors at various times along cardiac cycle